

PAPER

A novel low-frequency driving and high-speed motion stick-slip piezoelectric actuator based on two-stage compliant amplification mechanisms

To cite this article: Wanjiang Chen *et al* 2025 *Smart Mater. Struct.* **34** 075015

View the [article online](#) for updates and enhancements.

You may also like

- [A magneto-enhanced mechanical-dynamic model for isotropic soft magnetorheological elastomers and design of isolator with magnetically-controllable vibration bandgap](#)
Guangping Gong, Rui Li and Bochao Wang
- [Piezoelectric-based sole energy harvester for capturing energy from human walking](#)
Haisu Liao, Yidi Wang, Zhongliang Ren et al.
- [A micro-piezoelectric inertial robot with an ultra-high load-to-weight ratio: design and experimental evaluation](#)
Shichao Liang, Shuo Wang, Haoyu Gu et al.



The Electrochemical Society
Advancing solid state & electrochemical science & technology

UNITED THROUGH SCIENCE & TECHNOLOGY

248th ECS Meeting Chicago, IL October 12-16, 2025 *Hilton Chicago*





Science + Technology + YOU!

Register by
September 22
to **save \$\$**

REGISTER NOW

A novel low-frequency driving and high-speed motion stick-slip piezoelectric actuator based on two-stage compliant amplification mechanisms

Wanjiang Chen^{1,4}, Ruijie Li^{1,4}, Yitong Li¹ , Tingting Ye² and Zhao Feng^{1,3,*} 

¹ School of Power and Mechanical Engineering, Wuhan University, Wuhan 430072, People's Republic of China

² Department of Industrial and Systems Engineering, The Hong Kong Polytechnic University, Kowloon, Hong Kong Special Administrative Region of China 999077, People's Republic of China

³ Wuhan University Shenzhen Research Institute, Shenzhen 518057, People's Republic of China

E-mail: fengzhao@whu.edu.cn

Received 8 February 2025, revised 25 May 2025

Accepted for publication 23 June 2025

Published 9 July 2025



Abstract

Stick-slip piezoelectric actuators exhibit the advantages of simple structure, compact size, high resolution, and fast motion speed, enabling millimeter-scale motion range with nanometer-level positioning accuracy. Owing to these unique features, they hold strong potential for high-precision positioning in advanced microsystems, biomedical engineering, optical instrumentation, and other emerging technologies. However, current high-speed stick-slip piezoelectric actuators suffer from the problems of unstable motion, actuator damage, and contact wear due to the high-frequency driving. In this paper, by combining the parallelogram with the triangular mechanism, a two-stage compliant amplification mechanism is integrated into the stick-slip piezoelectric actuator to achieve low-frequency driving and high-speed motion simultaneously. Based on the compliance matrix method, a theoretical model is developed and utilized for structural optimization. Finite element analysis is conducted to verify its accuracy. The performance of the actuator is further investigated by testing the prototype. The experimental results demonstrate that a maximum motion speed of 20.51 mm s^{-1} is achieved under driving frequency of only 300 Hz and driving voltage of 100 V. Furthermore, the largest vertical load that the piezoelectric driver can support is 700 g when the locking force is 5 N. Compared with the previous studies, the proposed actuator presents good low-frequency driving and high-speed motion performance.

Keywords: piezoelectric actuator, stick-slip principle, compliant mechanisms, low-frequency driving, high-speed motion

⁴ Contributed equally to this work.

* Author to whom any correspondence should be addressed.

1. Introduction

As precision positioning technology, precision drive technology and micro operations technology becoming more and more important in the development of science [1, 2], piezoelectric actuators that can achieve high resolution, fast response and large driving force have been paid more attention and widely used [3, 4].

The piezoelectric actuator can be divided into direct driving piezoelectric actuator and stepping piezoelectric actuator according to different driving principles [5–8]. The limited stroke of lead zirconate titanate (PZT) stacks in direct driving actuators inherently narrows their viable application scope. Therefore, the stepping piezoelectric actuator which can realize infinite travel in theory has been studied and applied more widely [9]. Stepping piezoelectric actuators include ultrasonic piezoelectric actuators [10–12], inchworm piezoelectric actuators [13–15], and stick-slip piezoelectric actuators [16–18]. Ultrasonic piezoelectric actuators exhibit high operational speeds and driving frequencies, typically reaching tens of kilohertz. However, excessively high driving frequencies induce severe wear, significantly reducing the actuator's service life. The inchworm piezoelectric actuator delivers substantial output force. However, its operational principle necessitates multiple PZTs for motion generation, resulting in structural and control complexities. For large-stroke precision actuation or positioning applications, stick-slip piezoelectric actuators have attracted extensive research attention due to their advantages of compact structure, small size, high resolution, and simplified control system.

To further enhance the output performance of stick-slip piezoelectric actuators, numerous studies have been conducted. The maximum driving speed can be improved through increasing the driving frequency, minimizing backward motion, and enlarging step distance [19]. Increasing the drive frequency is the most straightforward approach to enhance driving speed, as it requires neither structural modifications nor sophisticated waveform design. Li *et al* proposed a novel stick-slip actuator based on a two-stage flexure hinge structure. The actuator's simple structure and large resonance frequency allow the actuator to achieve a maximum speed of 354.55 mm s^{-1} at a drive voltage of 150 V and a drive frequency of 4.7 kHz [20]. However, high frequency driving induce severe wear and shortened operational lifespan, thereby limiting the practical applicability of this method.

Reverse displacement during the stick phase is readily induced by commonly employed asymmetric sawtooth waveforms. Consequently, the reduction of backward motion has emerged as a critical research focus for enhancing actuator speed. Dong *et al* proposed a stick-slip piezoelectric actuator with an active locking mechanism (ALM). The ALM clamps the slider during the backward motion of the stick-slip actuator, thereby realizing suppression of backward motion, allowing the actuator to achieve a maximum speed of 2.26 mm s^{-1} at a drive voltage of 100 V and a drive frequency of 700 Hz [21]. Li *et al* designed a flexure beam to suppress the backward

motion of the actuator. This makes the actuator achieve a maximum speed of 23.714 mm s^{-1} at a drive voltage of 100 V and a drive frequency of 400 Hz [22]. Ding *et al* designed a stick-slip piezoelectric actuator with the alternating step approach. It reduces the backward motion during the piezoelectric actuator motion by two drive foot collaboration and also increases its motion speed. This enabled their stick-slip piezoelectric actuator to achieve 24.42 mm s^{-1} at a drive voltage of 100 V and a drive frequency of 1300 Hz [23].

Increasing the step distance also serves as an effective method for enhancing the motion speed. Lu *et al* amplified the lateral displacement of the structure by combining the asymmetric flexure hinge with the triangular displacement amplifying mechanism, realizing the function of increasing the step displacement. A maximum speed of 20.17 mm s^{-1} at a drive voltage of 100 V and a drive frequency of 610 Hz are achieved [19]. Huang *et al* designed a special L-shaped flexure hinge to amplify the output displacement of the actuator. This enables the actuator to achieve a maximum speed of 16.67 mm s^{-1} at a drive voltage of 100 V and a drive frequency of 800 Hz [24]. By combining the driving foot with the lever displacement amplification mechanism, a maximum speed of 11.21 mm s^{-1} at a drive frequency of 610 Hz was achieved [25]. Guo *et al* designed an asymmetric mechanism to increase the stepping displacement, which consists of two right circular flexure hinges and four leafspring flexure hinges. The presented mechanism achieved a peak speed of 26.2 mm s^{-1} at a drive voltage of 100 V and a drive frequency of 500 Hz [26]. A linear stick-slip piezoelectric actuator combining a two-stage amplification system with a Z-beam was proposed by in [27]. The actuator has good bi-directional motion capability and is capable of achieving a maximum speed of 12.88 mm s^{-1} at a drive voltage of 140 V and a drive frequency of 400 Hz.

In summary, while increasing the drive frequency induces severe wear and motion instability, and backward motion reduction offers limited speed improvement, increasing the step distance enables higher velocities at lower-frequency driving. Compliant amplification mechanisms enable displacement amplification of PZT outputs, achieving higher driving speeds while simultaneously avoiding the vibration, noise, and lifespan reduction issues associated with high-frequency operation. Structural optimization of the actuator enhances hardware-level performance to achieve millimeter-scale motion, while nano-scale positioning accuracy necessitates the implementation of control strategies. The positioning precision of piezoelectric-driven systems is adversely affected by interfacial frictional nonlinearities [28, 29] and intrinsic hysteresis nonlinearities inherent to PZT [30, 31]. Several friction models have been reported to address frictional nonlinearities and their impact on stick-slip dynamics. Hu *et al* proposed a slider-on-belt model to investigate stochastic planar stick-slip motions [32] and an explicit frictional contact algorithm incorporating the LuGre model to effectively account for the stick-slip dynamics [33]. Zhu *et al* investigated the effect of dynamic normal force on the stick-slip vibrations [34]. To achieve higher positioning accuracy, control methods are also

widely reported employing feedforward modeling to compensate for inherent nonlinearities and feedback control for real-time error correction [35, 36]. A universal optimization method for driving pulse is provided to determine the optimal parameters that enable stick-slip piezoelectric actuators to achieve stable motion at maximum velocity [37]. Overall, these modeling and control methodologies enable stick-slip piezoelectric actuators to achieve nanometer-level positioning accuracy, making them suitable for micro-nano operation applications. While this study primarily focuses on mechanical design and parametric optimization for enhanced open-loop performance, subsequent integration of advanced control strategies would further improve the actuator's dynamic capabilities.

Overall, in this paper, a novel low-frequency driving, high-speed motion stick-slip piezoelectric actuator based on a two-stage compliant amplification mechanism is proposed. The actuator integrates a parallelogram flexure hinge with a triangular amplification mechanism to constitute a novel compliant amplification mechanism. This amplification mechanism amplifies the output displacement of the actuator twice, which greatly increases the step displacement of the piezoelectric actuator, thereby increasing the speed of motion of the piezoelectric actuator at low-frequency driving. The main contents of the remaining sections of this paper are as follows: section 2 describes the structural design and working principle of the presented stick-slip piezoelectric actuator. In section 3, the theoretical modeling and parameters optimization are carried out, and finite element analysis (FEA) is conducted to verify the theoretical model. The experimental platform and motion performance tests are provided in section 4. The performance of the actuator is also compared with that of other stick-slip piezoelectric actuators. Conclusions are given in section 5.

2. Structure design and working principle of the actuator

2.1. Structure design of the actuator

As shown in figure 1(a), the PZT stack, the compliant amplification mechanism, the preload bolt, the slider, the connectors, the hand-adjustable platform, and the adjustment knob are the main components of the stick-slip piezoelectric actuator proposed in this paper. The PZT stack provides the input displacement, the compliant amplification mechanism transmits the input displacement to the slider and amplifies it, and preload bolts are used to adjust the preload force between the PZT stack and the compliant amplification mechanism. The slider acts as a mover to output linear displacement. The connector is used to fix the slider and the compliant amplification mechanism to the micro stage. The position of the hand-adjustable platform can be adjusted by an adjustment knob, and the preload force between the compliant amplification mechanism and the slider can be adjusted by changing the position of the hand-adjustable platform.

The structure diagram of the stator is shown in figure 1(b). The output displacement of the actuator is determined by the

stator, while the performance of the stator is mainly determined by the compliant amplification mechanism. The compliant amplification mechanism consists of a parallelogram flexure hinge and a triangular compliant amplification mechanism. When the PZT stack is vertically extended, the parallelogram flexure hinge produces a significantly amplified lateral displacement. This lateral displacement is then further amplified by the triangular compliant amplification mechanism and transmitted to the drive foot, which pushes the slider to slide. In addition, the compliant amplification mechanism will exert a shear force on the PZT stack during lateral displacement, and the PZT stack is susceptible to damage under the shear force. In this paper, a circular arc structure is designed to reduce the contact surface between the PZT stack and the compliant amplification mechanism, and can effectively reduce the shear force on the PZT stack.

2.2. Working principle

Figure 2 describes the working principle of the stick-slip piezoelectric actuator designed in this paper, divided into initial, stick and slip stage.

Step 1: initial stage $t = t_0$. As shown in figure 2(a), the drive foot of the compliant amplification mechanism is in contact with the slider with a certain initial pressure. This corresponds to the t_0 of the sawtooth wave signal, where the excitation voltage is zero, the PZT stack maintains its initial length, and the whole structure is at rest.

Step 2: stick stage $t = t_0 - t_1$. As shown in figure 2(b), the sawtooth wave voltage signal increases steadily from t_0 to t_1 while the PZT stack is slowly elongated by the voltage excitation. The parallelogram hinge in the compliant mechanism changes the displacement of the PZT stack in the vertical direction (i.e. x -axis direction) to a lateral displacement (i.e. y -axis direction), and due to the property of parallelogram hinge mechanism, it causes the lateral displacement to be significantly amplified. This lateral displacement is transmitted to the drive foot through the triangular amplification principle, thus pushing the slider to move. In this process, due to the tilted arrangement of the triangular amplification mechanism, a parasitic displacement in the vertical direction is generated in the drive foot during the transverse displacement, and the magnitude of the parasitic displacement varies with the magnitude of the transverse displacement. This allows that during the stick stage, the positive pressure of the drive foot on the slider becomes larger as the lateral displacement of the drive foot increases. Therefore, the presence of parasitic motion allows the slider to move forward steadily with the lateral displacement of the drive foot, defined as the step displacement S_1 .

Step 3: slip stage $t = t_1 - t_2$. As seen in figure 2(c), the sawtooth wave voltage signal rapidly decreases to 0 from t_1 to t_2 , and the PZT stack is excited by the voltage to rapidly contract and return to its original state. The flexure mechanism quickly releases the elastic potential energy due to the loss of the force of the PZT stack, and returns to its original state as the PZT

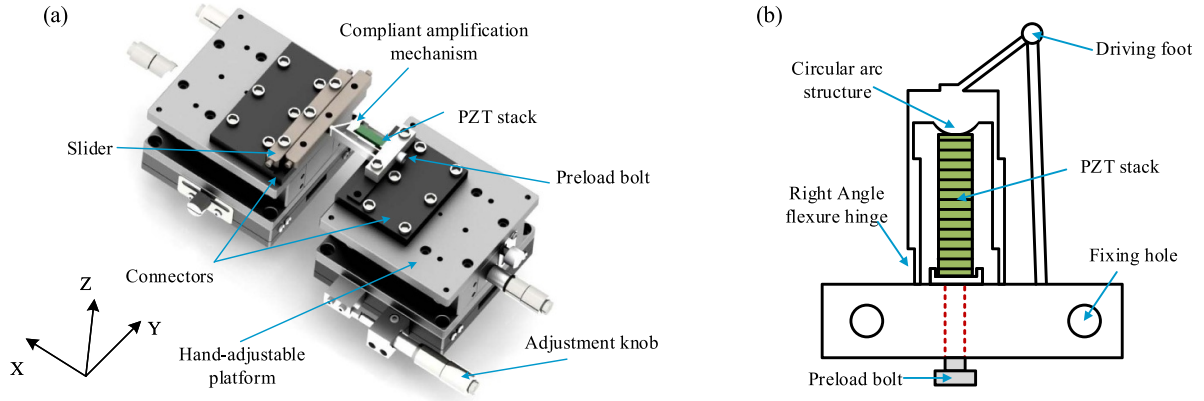


Figure 1. Structure design of the actuator. (a) The 3D model of the proposed stick-slip actuator; (b) structure diagram of the stator.

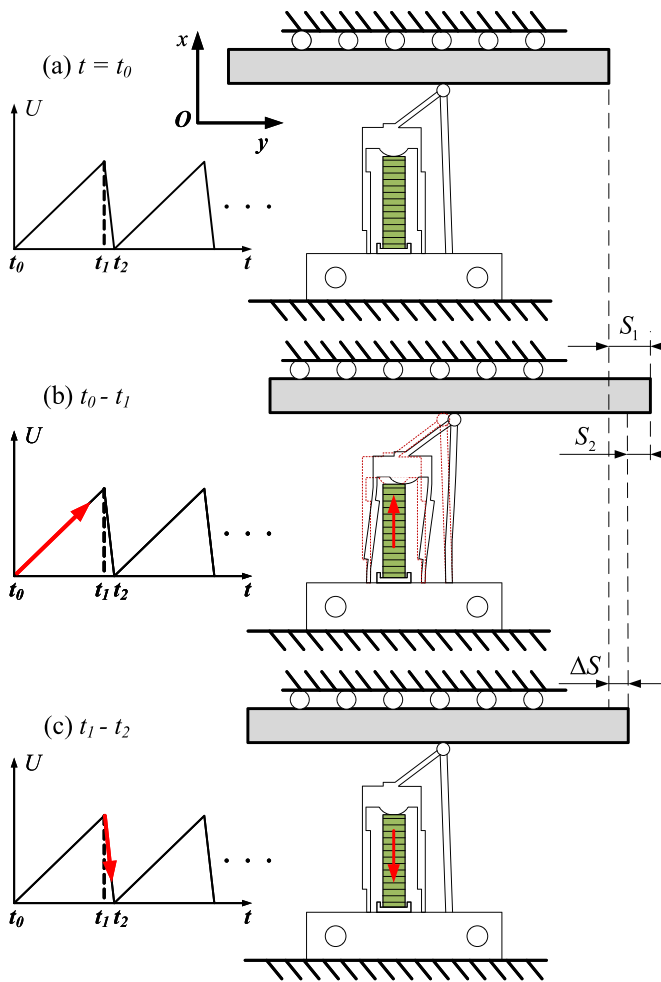


Figure 2. The actuator's working principle. (a) Initial stage $t = t_0$; (b) stick stage $t = t_0 - t_1$; (c) slip stage $t = t_1 - t_2$.

stack shrinks. Due to the rapid recovery of the compliant amplification mechanism, the drive foot quickly generates backward motion, but the slider will move forward due to the inertia. Therefore, the drive foot and the slider will produce relative sliding. At this time, the friction between the slider and

the drive foot will also be changed from stable static friction to sliding friction. The backward displacement of the slider due to sliding friction is defined as S_2 . In the process due to the existence of parasitic motion, the positive pressure of the drive foot on the slider will also be rapidly reduced with the backward displacement of the drive foot, and the reduction of the positive pressure can make the sliding friction between the slider and the drive foot also reduce, so as to realize the role of inhibiting backward motion.

The initial phase occurs only once during the entire drive process, and thereafter, by repeating sawtooth wave electrical signal that alternates the stick phase with the slip phase, the slider is able to realize continuous linear motion with infinite travel. At this point the primary stick and slip stages are one cycle, and the displacement forward in one cycle is the effective step displacement, defined as ΔS , where $\Delta S = S_1 - S_2$.

3. Structural modeling and analysis

3.1. Analytical modeling

The compliance matrix method has significant advantages in the kinematic modeling theory of the compliant amplification mechanism [38]. Therefore, in this paper, the compliant matrix method is adopted for the theoretical modeling. Since this compliance amplification mechanism is not subject to almost any forces and moments in the vertical plane direction, the planar flexure hinge with 3×3 compliance matrix is used to calculate the kinematic modeling.

The compliant amplification mechanism is mainly composed of a right-angle hinge. The structural parameters of the right-angle hinge are shown in the upper left corner of figure 3. It can be obtained that the end of the right-angle hinge will produce a small deformation δ when it is subjected to force. This deformation is calculated as $\delta = CF$, where C is the compliant matrix and F is the force on the end. In addition, the compliant matrix is related to the stiffness by the equation $C = k^{-1}$, so to calculate the input stiffness and output stiffness of a compliant amplification mechanism is equivalent to calculating its input compliance and output compliance. The δ is also considered

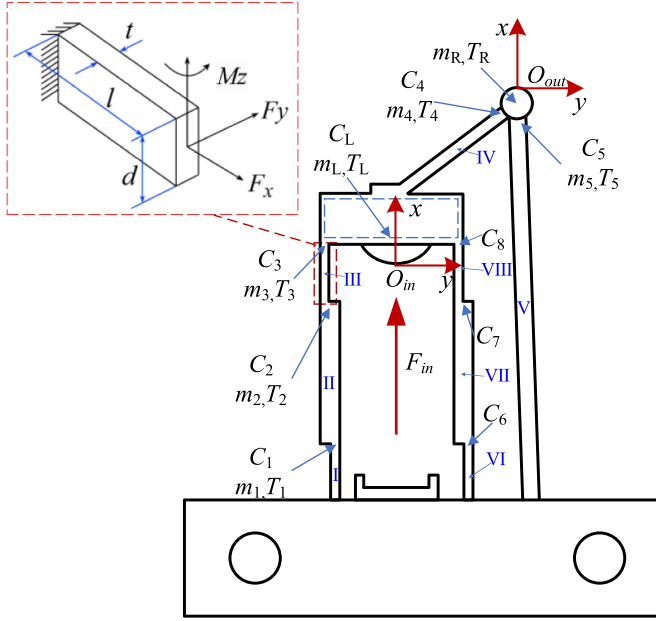


Figure 3. Coordinate diagram of plane flexure hinge mechanism.

as the output displacement at the end of the hinge and can be expressed in the compliance matrix as $\delta = [\delta_x \ \delta_y \ \delta_\theta]^T$. F is also considered as the input force, and the same can be expressed in the compliant matrix as $F = [F_x \ F_y \ M_z]^T$. The compliant matrix of the end of right-angle hinge can be expressed as

$$C_i = \begin{bmatrix} C_{x,F_x} & 0 & 0 \\ 0 & C_{y,F_y} & C_{y,M_z} \\ 0 & C_{\theta_z,F_y} & C_{\theta_z,M_z} \end{bmatrix} \quad (1)$$

where $C_{x,F_x} = \frac{l}{tdE}$, $C_{y,F_y} = \frac{4l^3}{t^3dE} + \frac{\alpha l}{Gtd}$, $C_{y,M_z} = C_{\theta_z,F_y} = \frac{6l^2}{t^3dE}$, $C_{\theta_z,M_z} = \frac{12l}{t^3dE}$. C_{x,F_x} represents the compliance for the deformation of a right-angled hinge end in the X direction when the force acts only in that direction. C_{y,F_y} represents the compliance for the deformation of a right-angle hinge end in the Y direction when the force acts only in that direction. C_{y,M_z} represents the compliance for a right-angle hinge deforming in the Y direction under the action of a moment in the Z direction. C_{θ_z,F_y} represents the compliance for a right-angle hinge deformed by bending around the z -axis under a force in the Y direction. t is the thickness of the right-angle hinge, l is the length, d is the width, E is the Young's modulus of the material, G is the shear modulus, and α is the shear modification factor, which is $\alpha = 6/5$ for a rectangular section.

The compliant amplification mechanism designed in this paper consists of multiple right-angle hinges connected in series and parallel, so calculating the input compliance and output compliance of the compliant amplification mechanism requires the superposition of the results of the compliance matrix of the deformation of all the right-angle hinge ends.

For a series flexure hinge, the global compliance of the series flexure hinge is the sum of the flexibility matrices of the individual flexure units (a right-angle hinge is considered

as a flexure unit in this paper) in the reference coordinate system. In other words, the end deformations of all flexure units in the local coordinate system are superimposed on the reference coordinate system by coordinate transformation to find the sum. Let the compliance matrix of each flexure unit in the series flexure hinge be denoted as C_{si} , then the compliance matrix C_s is calculated as follows:

$$C_s = \sum_{i=1}^n T_i^s C_{si} (T_i^s)^T \quad (2)$$

where $T_i^s = R_i^s P_i^s$ is the coordinate transformation matrix, given as:

$$R_i^s = \begin{bmatrix} \cos \theta_i^s & -\sin \theta_i^s & 0 \\ \sin \theta_i^s & \cos \theta_i^s & 0 \\ 0 & 0 & 1 \end{bmatrix} \quad (3a)$$

$$P_i^s = \begin{bmatrix} 1 & 0 & y_i^s \\ 0 & 1 & -x_i^s \\ 0 & 0 & 1 \end{bmatrix} \quad (3b)$$

where θ_i^s is the angle of counterclockwise rotation of the local coordinate system i with respect to the coordinate system s . The x_i^s and y_i^s are the coordinates of the position of the local coordinate system i in the coordinate system s . In the above method, the rest components are regarded as rigid bodies except for the flexure units.

For parallel flexure hinges, the load to achieve the same deformation is the sum of the loads required for each flexure unit, so the global stiffness matrix of the parallel flexure mechanism in the coordinate system is the sum of the stiffness matrices of each flexure unit. Let the compliance matrix of each flexure unit of the parallel flexure hinges be C_{pi} , then the compliant matrix C_p of the parallel flexure hinges is calculated as follows:

$$C_p = \left(\sum_{i=1}^n \left(T_i^p C_{pi} (T_i^p)^T \right)^{-1} \right)^{-1} \quad (4)$$

where T_i^p is the coordinate transformation matrix, which is calculated similarly to T_i^s .

So far, the compliant matrix calculation method for series flexure hinges and parallel flexure hinges has been obtained.

Based on the above method, the input stiffness of the compliant amplification mechanism is first calculated. Since the input of the compliant amplification mechanism is directly affected by the force, the input flexibility, and hence the input stiffness, can be directly calculated using a simple series-parallel flexure hinges compliance matrix method. In order to calculate the compliance matrix of the compliant amplification mechanism, the flexure hinge plane coordinate system is first constructed, as shown in figure 3. In the reference coordinate system O_{in} , let the input compliance matrix be C_{in} , given as:

$$C_{in} = \left((C_{s1})^{-1} + (C_{p1} + C_L)^{-1} \right)^{-1} \quad (5)$$

where C_{s1} represents the compliance matrix obtained by superimposing the end deformations of right-angle hinge IV and the right-angle hinge V through series connection at the input point O_{in} ; C_{p1} denotes the compliance matrix formed by parallelizing the end deformations of the two parallel sides of a parallelogram hinge mechanism at the input point O_{in} ; C_L is the compliant matrix of the input guide flexure beam. The expression of C_L is the same as that of C_i equation (1), with the difference that only $C_{x,F_x} = \frac{L^3}{4Et^3d}$ in the compliant matrix C_L , and the rest components are zero. This is because the input guide beam should be considered as a rigid body, but in actual calculations, it is found that the input guide beam would deform less in the input direction under the direct action of the force, so the compliance in the input direction is added to the calculation process as a way to get more accurate theoretical modeling results [39]. For C_{s1} and C_{p1} , their corresponding compliant matrices can be derived using equations (2) and (4), given as:

$$C_{s1} = T_4^{in} C_4 (T_4^{in})^T + T_5^{in} C_5 (T_5^{in})^T \quad (6)$$

$$C_{p1} = \left(\left(T_{s3}^{in} C_{s3} (T_3^{in})^T \right)^{-1} + \left(T_{s33}^{in} C_{s33} (T_{s33}^{in})^T \right)^{-1} \right)^{-1} \quad (7)$$

where C_4, C_5 represents the compliance matrix of the right-angle hinges IV and V; C_{s3} is the compliant matrix obtained by superimposing the end deformations of right-angle hinges I, II, and III in series at the end of right-angle hinge III; C_{s8} is the compliant matrix obtained by superimposing the end deformations of right-angle hinges VI, VII, and VIII in series at the end of right-angle hinge VIII. The corresponding compliance matrices are:

$$C_{s3} = T_1^{s3} C_1 (T_1^{s3})^T + T_2^{s3} C_2 (T_2^{s3})^T + T_3^{s3} C_3 (T_3^{s3})^T \quad (8)$$

$$C_{s8} = T_6^{s8} C_6 (T_6^{s8})^T + T_7^{s8} C_7 (T_7^{s8})^T + T_8^{s8} C_8 (T_8^{s8})^T \quad (9)$$

where C_i ($i = 1, 2, 3, 6, 7, 8$) represents the compliance matrix of the right-angle hinges I, II, III, VI, VII, VIII.

At this point, the calculations required for the input compliance matrix C_{in} have all been completed. If the input force of the PZT stack is F_x , the input displacement δ_{x-in} in δ_{in} can be expressed as:

$$\delta_{x-in} = C_{in} (1, 1) F_x. \quad (10)$$

Next, calculate the output stiffness of the compliant amplification mechanism. Since the deformation at the output position is not the position of the contact point of the force, and the series-parallel compliant matrix method calculates the force-displacement relationship at the same point, it is not possible to use the series-parallel compliant matrix method directly. In this paper, the computational model in [40] was referred to provide a theoretical basis. According to the over constraints of the closed-loop serial compliant mechanism, the internal forces act on the cross section and are truncated at the output point, as shown in figure 4. The deformation of the system cross-section at the left end of the figure 4 is as follows:

$$\delta_l = C_{gl} F_{gl} + \sum C_{iel} F_{iel} \quad (11)$$

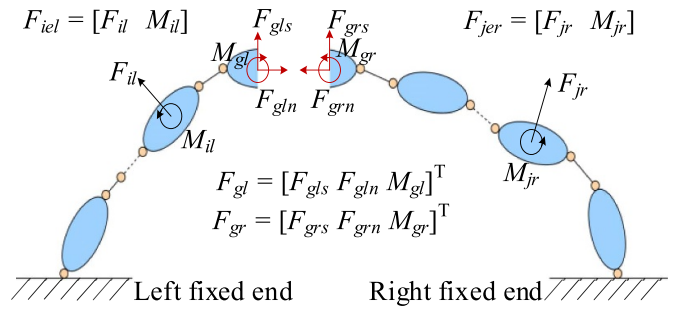


Figure 4. Closed-loop serial compliant mechanism stress diagram.

where C_{gl} is the compliance matrix of the internal force F_{gl} associated with the output point, and C_{gl} is the sum of the compliance of the compliant unit as it travels from the fixed end of the system at the left end to the point of internal force. C_{iel} is the compliance matrix of the external force F_{iel} associated with the displacement output point. The deformation of cross section at the right end of figure 4 is calculated as:

$$\delta_r = C_{gr} F_{gr} + \sum C_{jer} F_{jer} \quad (12)$$

where C_{gr} , F_{gr} , C_{jer} , and F_{jer} are the compliance and force matrices associated with the system at the right end, and their meanings are similar to those associated with the system at the left end.

The deformation and internal force of the cross-section has the following conditions: $\delta_l = \delta_r$, $F_{gl} = -F_{gr} = F_s$, and combining equations (11) and (12) yields the internal force of the cross-section F_s , which is solved as follows:

$$F_s = (C_{gl} + C_{gr})^{-1} (\sum C_{ier} F_{ier} - \sum C_{jel} F_{jel}). \quad (13)$$

Defining $B = C_{gl} + C_{gr}$ for ease of calculation, the deformation at the cross section is:

$$\delta_l = \sum (C_{gl} B^{-1} C_{ier}) F_{ier} - \sum (C_{gl} B^{-1} C_{iel} - C_{iel}) F_{iel} \quad (14a)$$

$$\delta_r = \sum (C_{gr} B^{-1} C_{iel}) F_{iel} - \sum (C_{gl} B^{-1} C_{jer} - C_{jer}) F_{jer}. \quad (14b)$$

Thus the deformation generated at the displacement output point when the compliant amplification mechanism is subjected to an external force is obtained as:

$$\begin{aligned} \delta_{out} &= \delta_l + \delta_r \\ &= \sum (C_{gr} B^{-1} C_{iel}) F_{iel} + \sum (C_{gl} B^{-1} C_{jer}) F_{jer}. \end{aligned} \quad (15)$$

According to the compliant amplification mechanism designed in this paper, it can be seen that the displacement output point O_{out} is the position where the drive foot contacts the slider. The left end is formed by the right-angle hinges I, II, III, IV, VI, VII, VIII and the input guide beam, and the external force $F_{iel} = F_{in} = [F_x \ 0 \ 0]^T$. The right end is the

right-angled hinge and the external force $F_{jer} = 0$. Therefore, the following displacement output is obtained:

$$\delta = \delta_{out} = (C_{gr}B^{-1}C_{iel})F_{in}. \quad (16)$$

From the above equation, we can get the output displacement of the compliant amplification mechanism by calculating C_{gl_out} , C_{gr_out} , C_{iel_out} and B , which can be solved as follows:

$$C_{gl_out} = T_{d_in}^{out}(C_{p1} + C_L)T_{f_out}^{p1} + T_{d_4}^{out}C_4T_{f_out}^4 \quad (17a)$$

$$C_{gr_out} = T_{d_5}^{out}C_5T_{f_out}^5 \quad (17b)$$

$$C_{iel_out} = T_{d_in}^{out}(C_{p1} + C_L)T_{F_in}^{in} \quad (17c)$$

$$B = C_{gl_out} + C_{gr_out} \quad (17d)$$

where $T_{d_i}^{out}$ is the displacement transformation matrix, for the displacement transformation matrix $T_{d_i}^{out} = P_i^{out}R_i^{out}$, the specific meanings of P_i^n and R_i^n are shown in equations (3a) and (3b). In $T_{f_out}^i$, f indicates that the matrix is an internal force transformation matrix. It transforms the internal force at the output point to the internal force at the local coordinate point by coordinate transformation $T_{f_out}^i = P_{out}^iR_{out}^i$. In $T_{F_in}^i$, F indicates that the matrix is an external force transformation matrix. The external force at the input point is transformed to the external force at the local coordinate point by $T_{F_in}^i = P_{in}^iR_{in}^i$.

At this point, the compliance matrix of the output point O_{out} is obtained as follows:

$$C_{out} = C_{gr}B^{-1}C_{iel}. \quad (18)$$

The output displacement is given as:

$$\delta_{y-out} = C_{out}(2,1)F_x. \quad (19)$$

According to δ_{in} and δ_{out} , the amplification A of the mechanism designed in this paper can be obtained as:

$$A = \frac{\delta_{y-out}}{\delta_{x-in}} = \frac{C_{out}(2,1)}{C_{in}(1,1)}. \quad (20)$$

In order to further obtain the structural performance of the compliant amplification mechanism, the theoretical calculation of its resonant frequency is also carried out and its dynamics was modeled using the Lagrange equation, expressed as:

$$\frac{d}{dt} \left(\frac{\partial T}{\partial \dot{q}_i} \right) - \frac{\partial T}{\partial q_i} + \frac{\partial V}{\partial q_i} = F_i \quad i = 1, 2, 3, \dots, n, \quad (21)$$

where T and V are the total kinetic and potential energies of the system, respectively; q_i denotes the generalized coordinates; N denotes the number of generalized coordinates, corresponding to the degrees of freedom of the system; and F_i denotes as the generalized non-conservative force. The input displacement variable δ_{in} is chosen as the generalized coordinate. Since the bending deformation of the right-angle hinge in the compliant amplification mechanism mainly occurs at the five positions of the right-angle hinge, I, II, V, VI and VII, the

rotational kinetic energy of these five parts needs to be calculated. Whereas right angle hinges III, IV, VII, input guide beams and drive foot mainly undergo translational displacements, the translational kinetic energy of these five sections was calculated. The kinetic energies of all the sections were added up to obtain the total kinetic energy T of the structure. Combined with the kinetic model in figure 3, the kinetic energy is derived as:

$$\begin{cases} T_1 = \frac{1}{2}J_1\omega_1^2 = \frac{m_1l_1^2(1+A_{in}^2)}{6(l_2^2+(l_1+l_2)^2)}\dot{\delta}_x^2 \\ T_2 = \frac{1}{2}J_2\omega_2^2 = \frac{m_2l_2^2(1+A_{in}^2)}{6(l_2^2+(l_1+l_2)^2)}\dot{\delta}_x^2 \\ T_3 = \frac{1}{2}m_3v_3^2 = \frac{1}{2}m_3(1+A_{in}^2)\dot{\delta}_x^2 \\ T_4 = \frac{1}{2}m_4v_4^2 = \frac{1}{2}m_4((1+A_x)^2 + (A_{in}+A)^2)\dot{\delta}_x^2 \\ T_T = \frac{1}{2}m_Tv_T^2 = \frac{1}{2}m_T(1+A_{in}^2)\dot{\delta}_x^2 \\ T_R = \frac{1}{2}m_Rv_R^2 = \frac{1}{2}m_R(A_x^2 + A^2)\dot{\delta}_x^2 \\ T_5 = \frac{1}{2}J_5\omega_5^2 = \frac{m_5(A_x^2+A^2)}{6}\dot{\delta}_x^2 \\ T_6 = T_1 \\ T_7 = T_2 \\ T_8 = T_3 \\ T = 2(T_1 + T_2 + T_3) + T_4 + T_T + T_R + T_5 \end{cases} \quad (22)$$

where m_i denotes the mass of each part of the compliant amplification mechanism, w_i denotes the rotational angular velocity of the bending of the right-angle hinge, and the rotational moment of inertia of the right-angle hinge can be denoted as J_i and $A_x = \frac{C_{out}(1,1)}{C_{in}(1,1)}$, $A_{in} = \frac{C_{in}(2,1)}{C_{in}(1,1)}$.

The virtual work concept states that the mechanism's potential energy can be written as follows:

$$V = \frac{1}{2}k_{in}\dot{\delta}_x^2. \quad (23)$$

Meanwhile, in the free vibration case, the external force $F_i = 0$, so the dynamic equation of the compliant amplification mechanism designed in this paper can be derived as:

$$m_e\ddot{\delta}_x + k_{in}\delta_x = 0 \quad (24)$$

where the equivalent mass $m_e = \frac{\partial T}{\partial \dot{\delta}_x} \frac{1}{\dot{\delta}_x}$ and the input stiffness $k_{in} = \frac{1}{C_{in}(1,1)}$. Finally, the resonant frequency of the flexure hinge mechanism is expressed as:

$$f = \frac{1}{2\pi} \sqrt{\frac{k_{in}}{m_e}}. \quad (25)$$

3.2. Parameter analysis and optimization

Dimensions are critical to the performance of a compliant amplification mechanism. The performance of the compliant amplification mechanism is mainly affected by the right-angle hinge. The structural parameters of the compliant amplification mechanism are shown in figure 5, where its main optimization parameters, $t_1, t_2, t_3, t_4, t_5, l_1, l_2, l_3, l_4, \theta$, are given. The design objective of this paper is mainly to increase the motion speed by increasing the stepping stroke, so the design optimization objective is to obtain the maximum magnification of

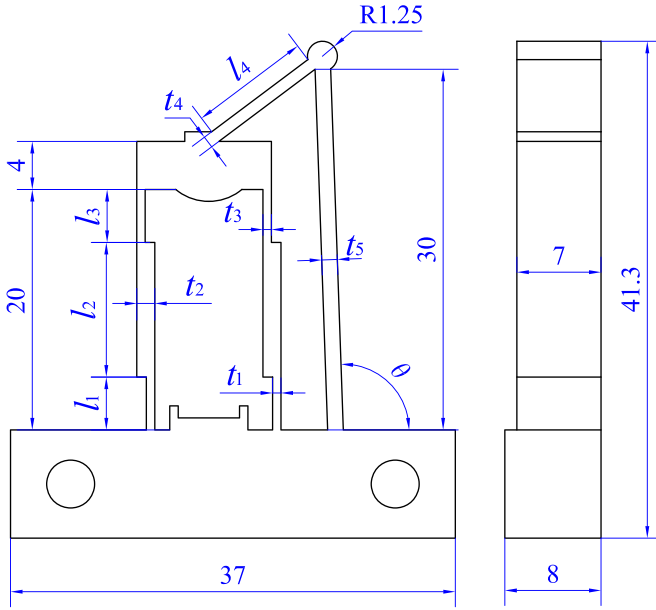


Figure 5. The structural parameters of the compliant amplification mechanism are shown for reference.

A. Due to the excessive number of optimization parameters and their mutual influence, this paper uses genetic algorithm to optimize the size of the designed mechanism. Taking into account the PZT stack dimensions, material properties, and other factors, the range of the parameters are specified as follows:

$$\begin{aligned} 0.5 \leq t_1 \leq 2 \text{ mm}, 1 \leq t_2 \leq 4 \text{ mm}, \\ 1 \leq t_4 \leq 2 \text{ mm}, 1 \leq t_5 \leq 2 \text{ mm}, \\ 3 \leq l_1 \leq 9 \text{ mm}, 10 \leq l_4 \leq 20 \text{ mm}. \end{aligned} \quad (26)$$

In order to ensure that right-angle hinges can realize a good enlargement function, the restriction on the ratio of the thicknesses of right-angle hinges I to the ratio of the thickness of II should be added. Moreover, to ensure that the compliant amplification mechanism has sufficient output displacement, the angle of inclination θ of the right-angle hinge is limited. Since the compliant amplification mechanism will be manufactured using wire-cut processing technology, a tolerance of 0.01 mm cannot be guaranteed, so the thinnest part of the right-angle hinge has to be less than 0.34 mm. Furthermore, considering the fatigue life of the structure, the thinnest part of the right-angle hinge is selected to be not less than 0.5 mm in this paper. Finally, considering the low operating frequency of the compliant amplification mechanism in this paper, in order to prevent the structure's resonant frequency from working with the driving frequency, the structure's resonant frequency is limited to not less than 1000 Hz. Overall, the boundary conditions in the process of calculations are shown as follows:

$$\begin{aligned} t_1 = t_3, l_1 = l_3 \\ l_1 + l_2 + l_3 = 20 \text{ mm}, 92^\circ \leq \theta \leq 95^\circ \\ 2 \leq t_2/t_1 \leq 3, f \geq 1000 \text{ Hz}. \end{aligned} \quad (27)$$

Table 1. Optimized structural parameters.

Structural dimension	t_1	t_2	t_3	t_4	t_5
Value (mm)	0.7	1.5	0.7	1	1.3
Structural dimension	l_1	l_2	l_3	l_4	θ
Value (mm)	4.4	11.2	4.4	10	92°

After considering the above factors, the structural dimensions of the compliant amplification mechanism are given in table 1. With this structural dimension, when an input force of 300 N is applied to the mechanism, the theoretical input displacement is calculated to be $20.50 \mu\text{m}$, while the corresponding output displacement reaches $224.39 \mu\text{m}$. This results in a theoretical maximum amplification ratio of $A_1 = 10.95$.

3.3. FEA

In order to further obtain the performance of the compliant amplification mechanism and to verify the reliability of the theoretical modeling results, the optimized compliant amplification mechanism was subjected to FEA using Ansys Workbench software. The theoretical maximum travel of the PZT stack is $20 \mu\text{m}$, and the input force in the simulation is set to 300 N, in order to bring the input displacement to its theoretical maximum. AL7075-T6 aluminum alloy is used for the compliant amplification mechanism. The material parameters of AL7075-T6 aluminum alloy are: density = 2810 kg m^{-3} , Young's modulus = 72 GPa, Poisson's ratio = 0.33, yield strength = 505 MPa.

Through static FEA, the results of directional deformation and equivalent stress were obtained when the input force was 300 N, as shown in the figure 6. Statics results show that the maximum displacement in the input direction is $21.194 \mu\text{m}$, the maximum displacement in the output is $219.75 \mu\text{m}$, and the input/output displacement amplification ratio is $A_2 = 10.37$. A comparative analysis between FEA results and theoretical predictions reveals the relative error of 3.3% for input displacement, relative error of 2.1% for output displacement, and relative error of 5.5% for displacement amplification ratio. Therefore, the theoretical results are valid with the FEA results. The maximum stress point in the structure is 115.98 MPa, which is much lower than the yield strength of AL7075 material 505 MPa. Modal analysis is also carried out, and the first four simulated modes are shown in the figure 7. The results illustrate that 1010 Hz is the first-order mode's native frequency, which meets the above constraint requirements, and it is evident that the platform's optimal dynamic properties are confirmed by the fact that the second-order natural frequency is more than twice as high as the first-order natural frequency.

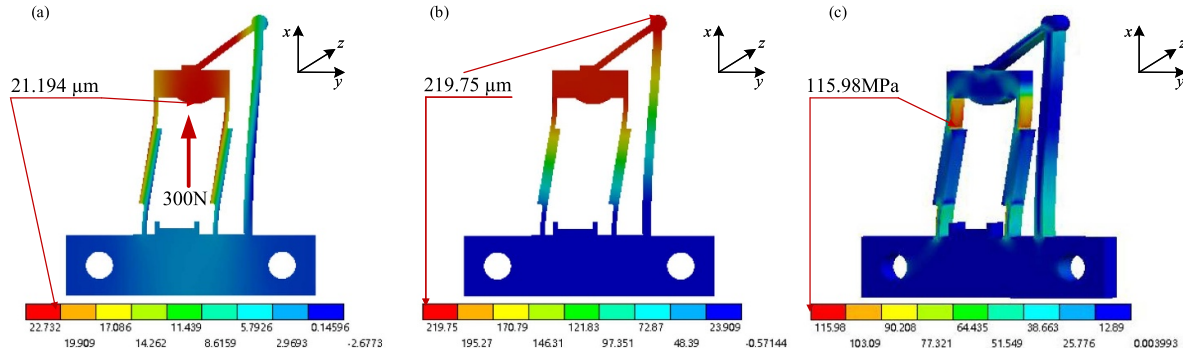


Figure 6. Finite element analysis results of the input and output displacements and stresses of the structure.

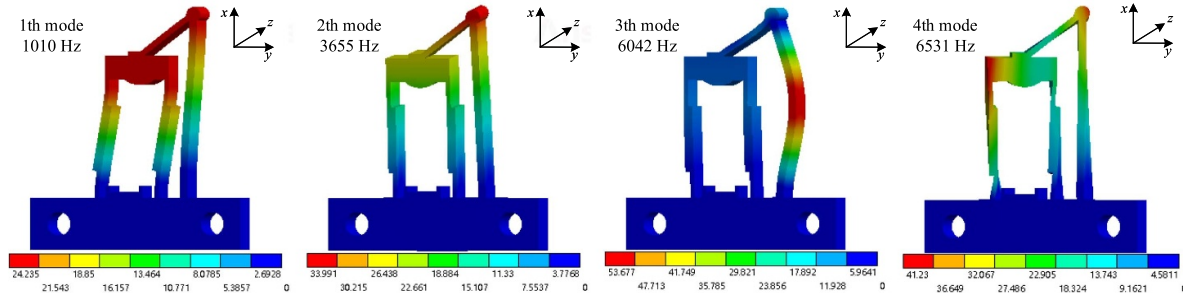


Figure 7. Finite element analysis results of modal analysis.

4. Experiments and discussion

4.1. Experimental setup

As shown in figure 8, the experimental platform of the stick-slip piezoelectric actuator was developed. The compliant amplification mechanism is fabricated by the wire electrical discharge machining, and the overall size is 37 mm×41.3 mm×8 mm. A hand-adjustable platform (Model: LE90-L-2, Shenzhen Huike Pneumatic Precision Machinery Co., LTD.) is used to adjust the preload between the drive foot and the slider. The test system uses a function signal generator (Model: DG1022, RIGOL, China) to provide a sawtooth wave voltage signal, which is amplified by a voltage amplifier (Model: E01, CORE MORROW, China) by a factor of 12 to drive the PZT stack (Model: PSt150/5×5/20L, CORE MORROW, China). The PZT stack then actuates the compliant amplification mechanism to drive the slider slide (Model: v3-75, THK, Japan). The output motion is measured using a laser displacement sensor (Model: LK-H025, Keyence Corporation, Japan). The test results are collected to a computer (PC) for further processing. In addition, the locking force of the mechanism is determined by weights, which are attached to the slider by means of fixed pulleys.

4.2. Experimental result

The displacement amplification ratios of the compliant amplification mechanism were first studied. A sawtooth signal with a voltage amplitude of 100 V, a driving frequency of 1 Hz,

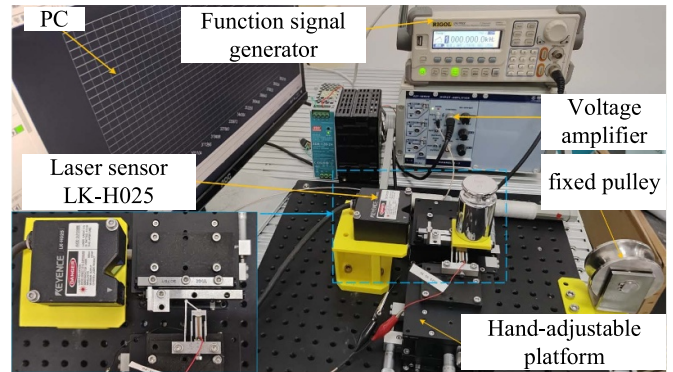


Figure 8. Test platform of the proposed stick-slip piezoelectric actuator.

and a signal with duty cycle of 0.95 was selected to excite the PZT stack (duty cycle of 0.95 was used for all subsequent excitation signal). Two orthogonal laser displacement sensors were used to measure the displacement of the input and output points simultaneously. The experimental results are shown in figure 9, with an input displacement of 6.76 μm and an output displacement of 75.67 μm, giving an actual amplification ratio of $A_3 = 11.19$. The actual amplification ratio $A_3 = 11.19$ has an error of about 2.2% compared with $A_1 = 10.95$ of the theoretical model, and an error of about 7.9% compared with the FEA result $A_2 = 10.37$. The comparison results show that the errors between the theoretical modeling and static simulation results are acceptable, which confirms the feasibility and rationality of the designed mechanism. In addition, we find

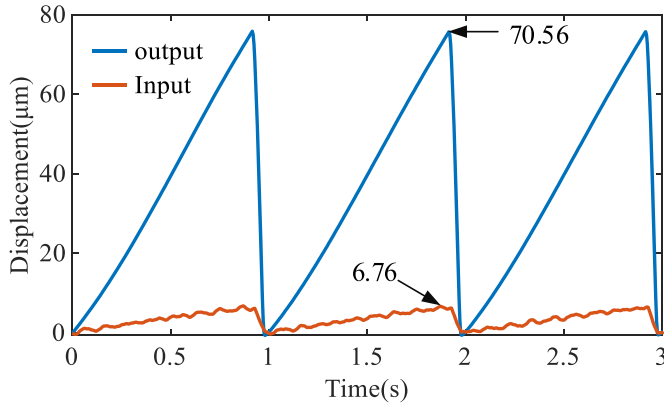


Figure 9. Test results of input and output displacement.

that the input displacement is less than $7 \mu\text{m}$. However, theoretically the input displacement of the PZT stack should be around $13 \mu\text{m}$ when the driving voltage is 100 V. The reason is that the PZT stack mounted on the compliant amplification mechanism is subjected to external forces. The theoretical displacement of the PZT stack is obtained without the influence of external forces. The force brought by the stiffness of the compliant amplification mechanism itself when the PZT stack is elongated. These external forces result in the actual input displacement of the PZT stack being much smaller than the theoretical input displacement.

The output performance of the prototype was then tested. The performance with different preload forces was first evaluated. It is difficult to measure the preload force directly, so considering the constant friction coefficient between the slider and the flexure hinge mechanism, the preload force can be adjusted indirectly by F_L locking force to F_N preload force. Adjust the locking force is shown in figure 10. The adjustment process is as follows: first, replace the weights, and then adjust the preload force between the prototype and the slider by turning the knob until the slider is about to slide, at which time the weight of the weights is the size of the locking force. After testing, the output speed results of the prototype with different locking forces are shown in figure 11. During the test, the driving voltage was 100 V and the driving frequency was 100 Hz. The results show that the output speed is slow when the locking force is small (e.g. 1 N, 2 N). This is due to the fact that the preload force between the driving foot and the slider is too small, and the poor contact between the two sides leads to the unstable motion of the stick stage of the stick-slip motion. When the locking force is 4 N, the actuator speed reaches a maximum value of 5.54 mm s^{-1} . In addition, the locking force of 4 N is used in all subsequent experiments. When the locking force is greater than 4 N, the actuator speed fluctuates within a range of about 4 mm s^{-1} .

Then, the results under different driving voltages were investigated, as shown in figure 12 by setting the driving frequency to 100 Hz. The figure 12(a) shows that the output speed of the actuator increases with the voltage and presents a good linear relationship. Therefore, it is possible to control the motion speed of the drive very well by changing the magnitude

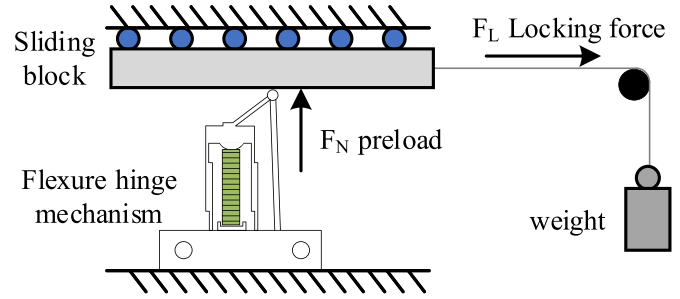


Figure 10. Diagram of locking force adjustment method.

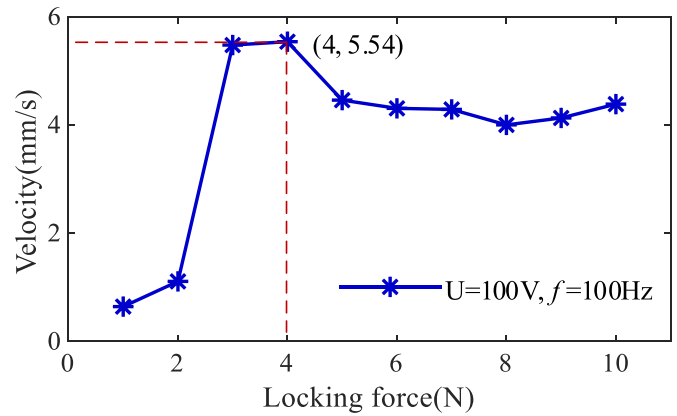


Figure 11. Effect of different locking forces on output speed.

of the input voltage. As illustrated in the figure 12(b), with the continuous increase of driving voltage, the effective step displacement ΔS of the actuator demonstrates a gradual ascending trend. Conversely, the backward motion displacement S_2 exhibits a non-linear variation pattern characterized by an initial decrease, followed by a subsequent increase, and ultimately a final decrease. In particular, when the driving voltage reaches 70 V, the backward motion displacement reaches its maximum value. This phenomenon provides experimental validation for the speed increase bottleneck observed at 70 V driving voltage in figure 12(a). In addition, it was found in the experiments that when the driving voltage was less than 15 V, it was difficult for the slider to maintain a stable motion. This is because the input force is too small and the slider is difficult to be pushed smoothly, indicating that the minimum drive voltage of the driver is 15 V. Figure 13 illustrates the step motion characteristics obtained under the minimum actuation voltage of 15 V. The measurements indicate that the actuator achieves a single-step effective displacement of $0.86 \mu\text{m}$ at 70 Hz. It is noteworthy that minor displacement fluctuations occur across consecutive motion cycles due to nonlinear friction effects. To quantify the impact of these fluctuations on overall motion accuracy, the cumulative displacement over 35 continuous motion cycles within 0.5 s was further calculated. The total displacement reaches $32.14 \mu\text{m}$, corresponding to an average effective displacement of $0.918 \mu\text{m}$. Consequently, the designed actuator demonstrates a motion resolution of approximately $0.918 \mu\text{m}$ under these operating conditions.

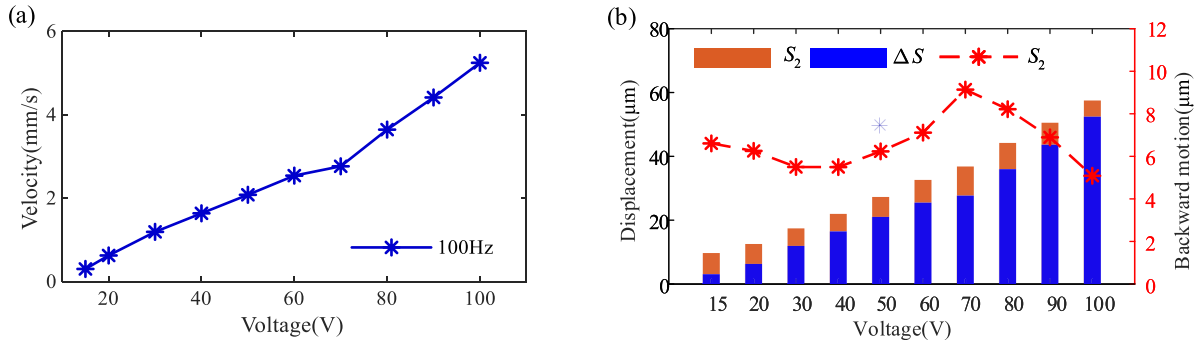


Figure 12. Test results at different drive voltages. (a) Effect of different drive voltages on output speed and (b) effect of different voltages on backward motion.

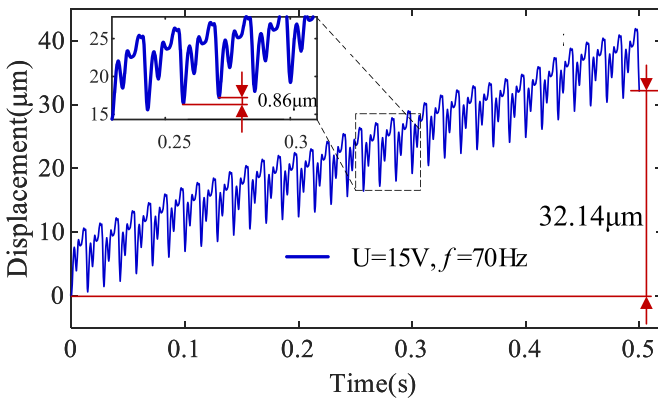


Figure 13. The motion resolution of the slider under a 15 V starting voltage.

Next, the effect of the drive frequency on the displacement and speed of the slider motion when the drive voltage is 100 V is investigated. From figure 14(a), it can be seen that when the driving frequency of the PZT stack does not exceed 300 Hz, the motion speed of the slider increases with the increase of the driving frequency with a certain linear relationship between them. When the drive frequency reaches 300 Hz, the slider movement speed reaches a peak value of 20.51 mm s^{-1} . Beyond a drive frequency of 300 Hz, the speed of motion begins to decrease and the relationship is no longer linear. This is because that the compliant amplification mechanism designed in this paper may reduce the output speed of the driver instead when the driving frequency exceeds 300 Hz. When the frequency is higher than a certain value, the compliant amplification mechanism does not have enough time to recover its initial state by its own elasticity before the PZT stack has already taken the next step in its elongation to push the compliant amplification mechanism again. This leads to a reduction in the step displacement of the compliant amplification mechanism and a corresponding reduction in the speed of the slider. Figure 14(b) shows that the output stepping displacement of the slider moves smoothly, which further verifies the reasonableness and reliability of the operating principle of the stick-slip piezoelectric actuator designed in this paper. As observed in figure 14(c), the backward

motion of the slider only occurs when the driving frequency is below 150 Hz, exhibiting a decreasing trend with increasing excitation frequency. This backward motion becomes completely suppressed when the frequency reaches or exceeds 150 Hz. Furthermore, the effective step displacement ΔS of the slider demonstrates a significant reduction when the driving frequency surpasses 300 Hz. Subsequent to this threshold, while the step displacement exhibits certain fluctuations with increasing frequency, its overall tendency shows a continued decline. These observed phenomena effectively explain the attenuation of speed fluctuations in the slider's motion profile beyond 300 Hz driving frequency as depicted in figure 14(a). Therefore, to get stable motion, the drive frequency can be selected between 150 and 300 Hz.

The stepping motion repeatability of the actuator was subsequently investigated through a series of controlled experiments. Each test protocol involved five sequential measurements at predetermined driving frequencies, with the relative average deviation calculated to quantify the stepping motion repeatability using the following expression:

$$\eta_s = \left[1 - \left(\sum_{i=1}^n \left| \frac{S_i - \bar{S}_n}{\bar{S}_n} \right| \right) / n \right] \times 100\% \quad (28)$$

where η_s denotes the stepping motion repeatability, n represents the number of repeated tests ($n = 5$ in this study), S_i corresponds to the cumulative displacement over 0.5 s in each individual test, and \bar{S}_n signifies the arithmetic mean of all S_i values. The experimental results summarized in table 2 reveal that while the repeatability gradually degrades with increasing driving frequency, the actuator maintains exceptional stepping consistency ($>94.96\%$) for frequencies up to 600 Hz. A dramatic decline to 75.85% repeatability is observed at 700 Hz operation, which is attributed to the onset of unstable stick-slip motion dynamics at elevated frequencies. This frequency-dependent performance characteristic indicates that the actuator demonstrates reliable stepping repeatability within the 600 Hz operational regime, with significant performance deterioration occurring at 700 Hz due to insufficient dynamic response time for proper stick-slip transition.

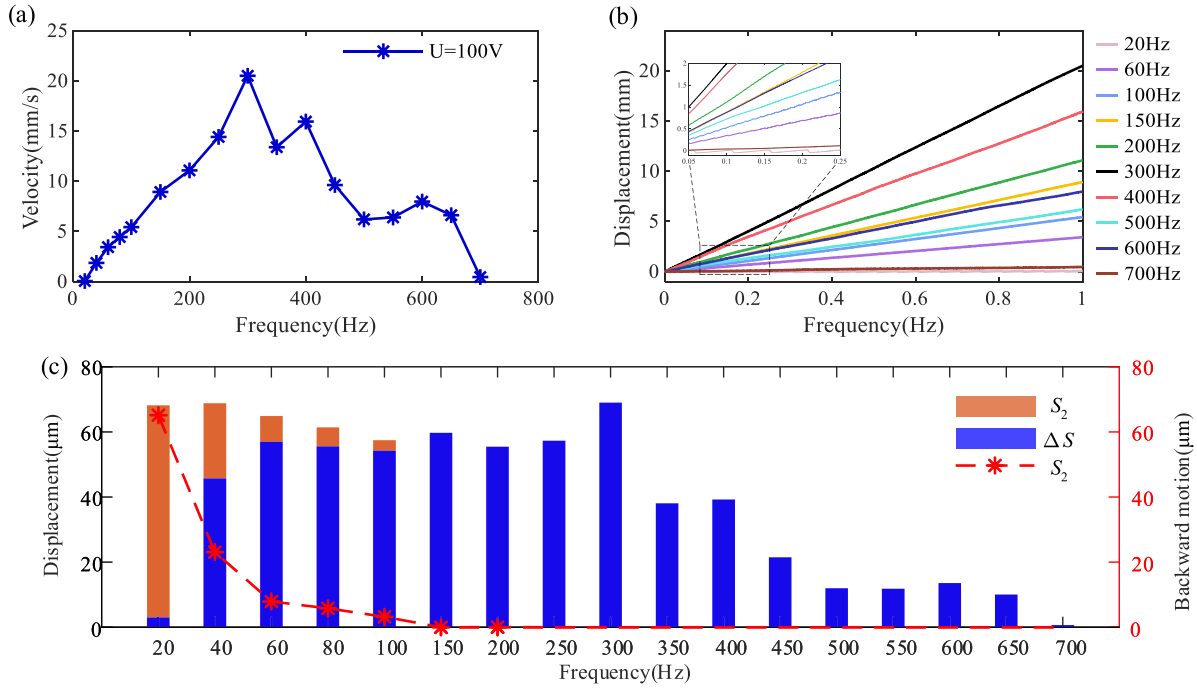


Figure 14. Test results at different drive frequencies. (a) Effect of frequency on speed and (b) effect of frequency on output displacement. (c) Effect of frequency on backward motion.

Table 2. Test results of step repeatability.

Drive frequency (Hz)	100 Hz	200 Hz	300 Hz	400 Hz	500 Hz	600 Hz	700 Hz
Step repeatability (%)	99.73	99.42	98.37	97.96	96.07	94.96	75.85

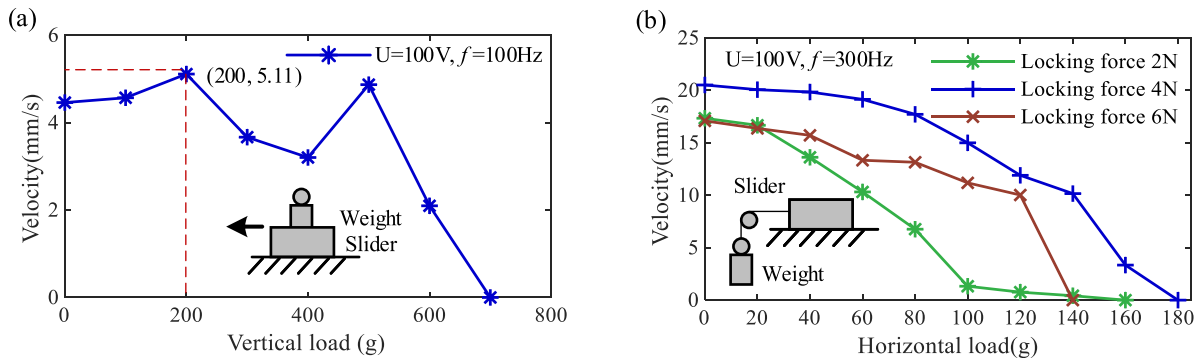


Figure 15. Test results at different loads. (a) Effect of different vertical loads on output speed and (b) effect of different horizontal loads on output speed.

Finally, experimental tests were conducted to evaluate the load performance of the piezoelectric actuator, with particular focus on investigating the effects of vertical and horizontal loads on output speed. The influence of vertical load on output speed is systematically analyzed in figure 15(a). When the voltage amplitude is set to 100 V and the driving frequency is 100 Hz, the output speed of the slider varies nonlinearly with the vertical load as the vertical load gradually increases. This is because the presence of the vertical load changes the preload force between the drive foot and the slider. When the vertical load reaches 200 g, the speed

of the slider can reach 5.11 mm s^{-1} , which is the maximum speed when the load acts on the slider. When the load exceeds 700 g, the speed of the slider becomes zero, indicating that the maximum vertical load capacity of the piezoelectric actuator is about 700 g. The influence of horizontal load on the slider's output speed is depicted in figure 15(b). When operating at 100 V voltage amplitude and 300 Hz driving frequency, the slider's output speed exhibits a gradual decrease with increasing horizontal load. Under locking forces of 2 N, 4 N, and 6 N, the actuator demonstrates maximum horizontal load capacities of 160 g, 140 g, and 180 g respectively. It is

Table 3. Performance comparisons with previous studies.

Reference	Driving voltage (V)	Driving frequency (Hz)	Speed of motion (mm s^{-1})	Resolution displacement (μm)	Amplification ratio	Horizontal load (g)	Vertical load (g)	Backward motion
[21]	100	700	2.26	/	1.95	160	/	No
[23]	100	1300	24.42	6.10	1.80	50	50	No
[19]	100	610	20.17	/	2.53	240	/	Yes
[24]	100	800	16.67	0.11	2.64	300	/	/
[25]	100	610	11.21	/	2.89	78	/	Yes
[26]	100	500	26.2	/	3.16	250	/	Yes
[27]	140	400	12.88	0.26	14.8	35	/	Yes
This work	100	300	20.51	0.918	11.19	180	700	No

noteworthy that the maximum load-bearing capacity does not monotonically increase with locking force. This counterintuitive phenomenon arises because excessive locking force significantly increases the friction between the slider and compliant amplification mechanism, thereby hindering the stick-slip motion required for effective actuation.

4.3. Discussion

Table 3 collects some previous high-speed stick-slip piezoelectric actuators and the low-frequency high-speed piezoelectric actuator designed in this paper for performance comparison. The proposed stick-slip actuator can reach a motion speed of 20.57 mm s^{-1} only at a driving frequency of 300 Hz under the condition of a relatively stable driving voltage. Compared with the previous high-speed stick-slip piezoelectric actuators, the piezoelectric actuator proposed in this paper has an obvious advantage in both low-frequency and high-speed motions. Positioning resolution was not compared because this paper has not yet addressed the control challenges posed by stick-slip nonlinearities and other disturbances. The integration of control strategies will be completed in our future work.

5. Conclusion

This paper presents the structural design, theoretical analysis and experimental test of a new type of low-frequency-driven high-speed motion stick-slip piezoelectric actuators based on a two-stage flexure amplification mechanism. By increasing the stepping displacement, the motion speed of the actuator is improved, and the low-frequency and high-speed motion performance is realized. The working principle and working process of the actuator designed in this paper are described, and the theoretical model of the compliant amplification mechanism is established by using the compliance matrix method, and the key parameters of the compliant amplification mechanism are optimized on this basis. The FEA is used to verify the accuracy of the theoretical model and determine the performance of the actuator. Then the prototype is fabricated and the test platform is built. The experimental results show that the actuator presents good motion stability and the speed increases

linearly with the increase of driving voltage. When the driving voltage is 100 V, only the 300 Hz driving frequency is needed to achieve the maximum motion speed of 20.51 mm s^{-1} . In addition, the experimental results show that the vertical load of 700 g is the maximum load of the stick-slip piezoelectric actuator designed in this paper. By comparing with previous piezoelectric actuators, we can conclude that the piezoelectric actuator proposed in this paper has excellent performance in realizing low-frequency and high-speed motion.

Data availability statement

The data cannot be made publicly available upon publication because no suitable repository exists for hosting data in this field of study. The data that support the findings of this study are available upon reasonable request from the authors.

Acknowledgments

This work was supported by National Natural Science Foundation of China (Grant No. 52405034), in part by Hubei Provincial Natural Science Foundation of China (Grant No. 2024AFB126), in part by Knowledge Innovation Program of Wuhan–Shuguang Project (Grant No. 2023010201020252), and in part by Guangdong Basic and Applied Basic Research Foundation (Grant No. 2023A1515110156), and in part by Aeronautical Science Foundation of China (Grant No. ASFC202400020S5001).

References

- [1] Liang C, Wang F, Huo Z, Shi B, Tian Y, Zhao X and Zhang D 2019 *IEEE Trans. Ind. Electron.* **67** 6963–74
- [2] Wang L, Jin J, Zhang H, Wang F and Jiang Z 2020 *Mech. Syst. Signal Process.* **135** 106183
- [3] Wang L, Chen W, Liu J, Deng J and Liu Y 2019 *Mech. Syst. Signal Process.* **133** 106254
- [4] Zhang Z, An Q, Li J and Zhang W 2012 *Int. J. Adv. Manuf. Technol.* **62** 669–85
- [5] Liu R, Wen Z, Cao T, Lu C, Wang B, Wu D and Li X 2022 *Precis. Eng.* **76** 226–36
- [6] Wang F, Shi B, Huo Z, Tian Y and Zhang D 2021 *Precis. Eng.* **68** 1–9

- [7] Wang Y, Xu Z and Huang H 2020 *Smart Mater. Struct.* **29** 125006
- [8] Mohith S, Upadhyaya A R, Navin K P, Kulkarni S and Rao M 2020 *Smart Mater. Struct.* **30** 013002
- [9] Li J, Huang H and Morita T 2019 *Sens. Actuators A* **292** 39–51
- [10] Ryndzionek R and Sienkiewicz L 2021 *Ultrasonics* **116** 106471
- [11] Ryndzionek R, Sienkiewicz L, Michna M and Kutt F 2019 *Sensors* **19** 5184
- [12] Yang C P, Xie K J and Chang J Y 2020 *Microsyst. Technol.* **26** 71–78
- [13] Ma X, Liu Y, Deng J, Gao X and Cheng J 2023 *Mech. Syst. Signal Process.* **184** 109704
- [14] Song S, Shao S, Xu M, Shao Y, Tian Z and Feng B 2018 *Sens. Actuators A* **282** 174–82
- [15] Yu S, Liang J, Yang F, Wang H, Liu X, Xu C, Wang Z and Xu D 2023 *Smart Mater. Struct.* **32** 055020
- [16] Li H, Wang J, Xu Z, Qin F, Wang Z, Zhu H and Zhao H 2023 *Mech. Syst. Signal Process.* **186** 109752
- [17] Wang J, Huang H, Zhang S, Qin F, Wang Z, Liang T and Zhao H 2020 *Mech. Syst. Signal Process.* **145** 106895
- [18] Duan B, Hu H, Lei Y and Chen J 2023 *Mechatronics* **95** 103067
- [19] Lu X, Gao Q, Li Y, Yu Y, Zhang X, Qiao G and Cheng T 2020 *IEEE Access* **8** 6515–22
- [20] Li Z, Zhao L and Yu X 2020 *Rev. Sci. Instrum.* **91** 055006
- [21] Dong J, Zhang B, Li X, Xu Z, Wang J, Liu C and Cao Y 2021 *Smart Mater. Struct.* **30** 095015
- [22] Li H, Wang J, Xu Z, Qin F, Wang Z and Zhao H 2023 *J. Intell. Mater. Syst. Struct.* **34** 364–76
- [23] Ding Z, Dong J, Zhou X, Xu Z, Qiu W and Shen C 2022 *Mech. Syst. Signal Process.* **181** 109494
- [24] Huang H, Xu Z, Wang J and Dong J 2020 *Smart Mater. Struct.* **29** 065007
- [25] Tian X, Yang J, Gai H, Li J, Wang Z, Dai Y and Niu D 2024 *IEEE Access* **12** 75199–207
- [26] Guo Z, Tian Y, Zhang D, Wang T and Wu M 2019 *Mech. Syst. Signal Process.* **128** 37–49
- [27] Xu D, Liang T, Cao C, Wang Z, Zhao Z and Yu S 2024 *Smart Mater. Struct.* **33** 115012
- [28] Nguyen H X, Edeler C and Fatikow S 2012 *Phys. Mesomech.* **15** 280–6
- [29] Zhang Q, Chen X, Yang Q and Zhang W 2012 *Int. J. Adv. Manuf. Technol.* **61** 1029–34
- [30] Wu Y, Chen J, Fan Y, Li L and Jiang Z 2024 *Mech. Syst. Signal Process.* **215** 111450
- [31] Špillar M and Hurák Z 2011 *Mechatronics* **21** 100–8
- [32] Hu H, Batou A and Ouyang H 2023 *Mech. Syst. Signal Process.* **183** 109572
- [33] Hu H, Zhu X, Batou A and Ouyang H 2024 *Nonlinear Dyn.* **112** 16061–80
- [34] Zhu Y, Wang R, Xiang Z, Mo J and Ouyang H 2022 *Nonlinear Dyn.* **110** 69–93
- [35] Oubellil R, Voda A, Boudaoud M and Régnier S 2019 *Sens. Actuators A* **285** 258–68
- [36] Zhang Z, Dong Y, Yu S, Lu X and Liu K 2023 *Sensors* **23** 7795
- [37] Neuman J, Nováček Z, Pavera M, Zlámál J, Kalousek R, Spousta J, Dittrichová L and Šíkola T 2015 *Precis. Eng.* **42** 187–94
- [38] Cao J, Ling M, Inman D J and Lin J 2016 *Smart Mater. Struct.* **25** 095005
- [39] Li J, Yan P and Li J 2019 *Mech. Sci.* **10** 299–307
- [40] Wang L P, Jiang Y and Li T M 2017 *Chin. J. Mech. Eng.* **30** 951–62